Finite Set Model Predictive Current Control for Variable Flux Memory Machine With a Novel Three-Layer Optimization Strategy

Xing Liu, *Graduate Student Member, IEEE*, Hui Yang, *Senior Member, IEEE*, Heyun Lin, *Senior Member, IEEE*, Feng Yu, *Member, IEEE*, and Yong Yang, *Senior Member, IEEE*

***Abstract*—Variable flux memory machine (VFMM) with changeable permanent magnet (PM) flux is recognized as a promising candidate in wide-speed-range applications. Because the electromagnetic parameters of VFMMs normally change with working conditions, the design of the current controller is very demanding in terms of robustness. For this reason, an improved finite-set model predictive current control (FS-MPCC) is proposed in this article. On one side, a simple measuring procedure is designed to obtain the susceptible parameters, including PM flux and *dq*-axis inductances. The obtained data are stored in look-up tables to online update the parameters involved in the prediction model so that the robustness of FS-MPCC can be significantly enhanced. On the other side, to improve the steady-state performance, the original control set is extended by a geometric modulation method. A novel three-layer optimization strategy is then proposed to select the optimal choice from the extended control set, effectively reducing the computational burden. In addition, an improved mathematical model is presented to deal with the induced voltage caused by the rapidly varied PM flux, which is a unique issue that exists in VFMM drives. Finally, the experimental results based on a prototype test rig validate the proposed FS-MPCC.**

***Index Terms*—Finite-set model predictive current control (FS-MPCC), model predictive control (MPC), parameter measurement, permanent magnet (PM), variable flux memory machine (VFMM).**

Manuscript received 4 December 2023; revised 7 April 2024; accepted 13 May 2024. Date of publication 22 May 2024; date of current version 16 July 2024. This work was supported in part by the National Natural Science Foundation of China under Grant 52037002 and Grant 52077033, in part by the Key R&D Program of Jiangsu Province under Grant BE2021052, in part by the "Thousand Talents Plan" Project of Jiangxi Province under Grant jsxq2020102088, in part by the Postgraduate Research & Practice Innovation Program of Jiangsu Province under Grant KYCX24_0394, and in part by Jiangsu Provincial Key Laboratory of Smart Grid Technology and Equipment, Southeast University. Recommended for publication by Associate Editor R. Kennel. *(Corresponding author: Hui Yang.)*

Xing Liu, Hui Yang, and Heyun Lin are with the School of Electrical Engineering and the Jiangsu Provincial Key Laboratory of Smart Grid Technology and Equipment, Southeast University, Nanjing 210096, China (e-mail: lyousying@seu.edu.cn; huiyang@seu.edu.cn; hyling@seu.edu.cn).

Feng Yu is with the School of Electrical Engineering, Nantong University, Nantong 226019, China (e-mail: yufeng628@ntu.edu.cn).

Yong Yang is with the School of Rail Transportation, Soochow University, Suzhou 215131, China (e-mail: yangy1981@suda.edu.cn).

Color versions of one or more figures in this article are available at https://doi.org/10.1109/TPEL.2024.3404038.

Digital Object Identifier 10.1109/TPEL.2024.3404038

I. Introduction

A. Research Background

PERMANENT magnet (PM) machines have attracted more and more attention in the industry [1], [2], [3], owing to their advantages like high power density, good reliability, and increasing efficiency. A troublesome impeding factor of further development of conventional PM machines is unchangeable PM flux, which results in the demerits of limited speed range and narrow high-efficiency region [4], as shown in Fig. 1(a). Especially, in high-speed regions, the flux-weakening operation realized by continuously injecting a negative *d*-axis current must be activated to reduce the back electromotive force (EMF) value, accompanied by a severe efficiency degradation [5]. To address this issue, variable flux PM machines have emerged and received growing interest, such as variable flux memory machines (VFMMs) [6], [7], [8], [9], [10], [11], [12], [13], [14], [15], [16].

The most pronounced property of VFMMs is the employment of low coercive force (LCF) PMs [6], like AlNiCo and SmCo magnets. The LCF PMs can be easily re-/demagnetized by applying a short current pulse. From this fact, the purpose of flux-weakening in high-speed regions can be realized with negligible copper losses [7]. Moreover, the feature of changeable PM flux is advantageous for maintaining high-efficiency operation in varied operating situations. The typical curves of torque/power versus speed of VFMMs are shown in Fig. 1(b), exhibiting two advantages in terms of wider speed range and wider high-efficiency region. Due to these advantages, VFMMs are especially suitable for applications with the requirement of wide-speed range, such as electric vehicles [8] and household appliances (e.g., washing machines [9], [10]).

B. Literature Review

The original concept of VFMM was introduced in [11] and only AlNiCo PMs are employed in the prototype. It is inevitable that the torque density of the original VFMM is relatively low. To tackle this issue, various topologies integrating both high coercive force (HCF) and LCF PMs in the rotor have been proposed [8], [12], [13], [14], [15]. The arrangement of two kinds of PMs is multifarious, and the resultant magnetic circuit can be of parallel type [12], series-type [8], or hybrid type [13]. It has been proven

that the parallel-type magnetic circuit suffers from the risk of unintended demagnetization of LCF PMs and the series-type one is subjected to the deficiency of a narrow flux-regulation range [14]. Comparatively, the hybrid-type magnetic circuit (HMC) is more attractive, since it combines the advantages of both parallel-type and series-type designs, as successfully verified in [13] and [15]. Compared to traditional PM machines, VFMMs normally have a relatively complicated rotor design and hence more apparent magnetic saturation effect [16]. As a result, their PM flux and *dq*-axis inductances show wide-range variations under different working conditions. Thus, the current controller should be highly robust to these electromagnetic parameters. Besides, the current controller also desires a very quick response to deal with the control of the *d*-axis current pulse for adjusting PM flux [17].

There have been some publications [17], [18], [19], [20], [21], [22] posing the concern on the control of VFMM drives. In [18], a maximum-torque-per-ampere technique based on a neural network is described, where the stator currents are regulated by using the standard vector control. In [19], the deadbeat (DB)–direct torque and flux control is used, which is an enhanced version of direct torque control (DTC). In [20], a modified model is established by considering the induced voltages during flux-regulation processes, and then an improved feed-forward current controller is proposed. The controller is heavily dependent on machine parameters, which are obtained by using the finite-element (FE) method. Differently, with the experimental measurement, the *dq*-axis inductances, cross-magnetization effects, torque-ripple, and torque-angle characteristics of a VFMM prototype are obtained by using the voltage injection method on the mature vector control framework [21]. Recently, the disturbance observer-based control methods have been studied for VFMM drives. In [17], an improved DB current control (DBCC) is proposed and applied to a dual three-phase VFMM drive. A disturbance observer is proposed to deal with the system uncertainties. In [22], a feed-forward current controller based on linear active disturbance rejection control is proposed. The embedded linear extended state observer is responsible for estimating the total disturbance, including the induced voltage resulting from the change of PM flux and the uncertainties due to parameter mismatches. Overall, two main control frameworks, namely vector control and DTC, have been extended to VFMM drives. Besides, either a parameter compensation scheme or disturbance observation technique can be utilized for the robustness enhancement.

C. Motivation and Contributions

With the advancement of modern microprocessors, model predictive control (MPC) strategies are of growing research interest and have been regarded as a new high-performance control framework for electrical machine drives. Among several MPC strategies, finite-set model predictive current control (FS-MPCC) is the most promising one, because of its explicit principle, simple implementation, and unique capability to handle nonlinearities and/or multivariables [23], [24]. FS-MPCC is outstanding in terms of dynamic performance [25], which

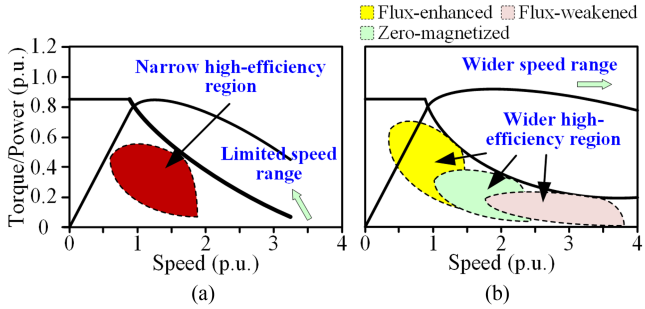

Fig. 1. Typical curves of torque/power versus speed of (a) traditional PM machines and (b) VFMMs.

is exactly fit for VFMM drives. This point encourages the motivation of our work, to make an attempt to apply FS-MPCC to VFMM drives. There are three issues that shall have attention as follows.

First, as a model-based control strategy, FS-MPCC extremely relies on the accuracy of machine parameters [26]. The most noteworthy issue is how to enhance the robustness of the system against the complicated parameter variations. As mentioned above, the parameter compensation scheme based on either the FE method [20] or experimental measurement [21] is a good choice to improve the robustness without complicating the total control program, differing from the schemes with parameter identification technique [27] or disturbance observer [26]. In this work, the parameter compensation method based on experimental measurement is adopted to deal with the parameter variations of VFMMs. A subsequent challenge is to measure the system parameters offline and to construct the associated look-up tables (LUTs), which is extremely time-consuming. Therefore, a simple measuring procedure of electromagnetic parameters including PM flux and *dq*-axis inductances is designed. It consists of two parts: 1) obtaining the PM flux and *d*-axis inductance with the aid of the voltage injection method [21]; and 2) identifying the *q*-axis inductance based on a flux observer.

Second, a distinctive issue that existed in VFMMs is the induced voltage caused by the rapid change of PM flux, as pointed out in [20] and [22]. The induced voltage can be modeled by adding a term of the differential of PM flux with respect to time (namely $d\psi_{\mathrm{PM}}/dt$) into the *d*-axis voltage equation [20]. However, such a modeling method is not applicable to FS-MPCC, as an additional state variable appears. This unique issue is tackled by using an improved mathematical model in this work. In short, the term $d\psi_{\mathrm{PM}}/dt$ is approximated as the product of a linearly equivalent inductance and di_{d}/dt so that the induced voltage is easily integrated into the original mathematical model. As such, the control performance during flux-regulation processes can be further improved.

Third, the steady-state performance of FS-MPCC does not bear comparison with the modulation-based vector control [28]. One way around this problem is to increase the number of options in the control set by constructing virtual vectors, usually accompanied by increased computational burden. Therefore, some effective optimization strategies have been proposed [29],

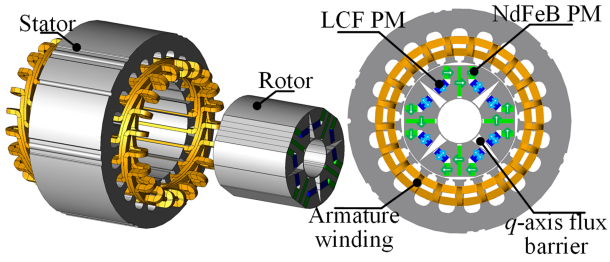

Fig. 2. Topology of the investigated HMC-VFMM.

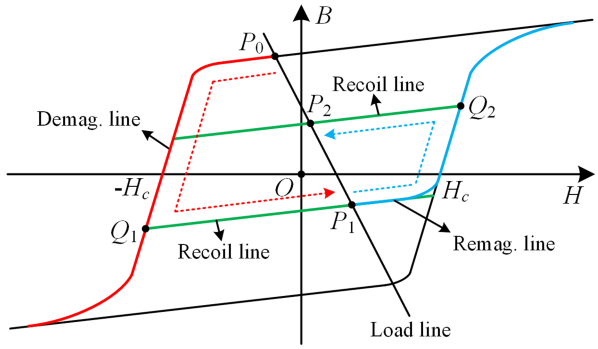

Fig. 3. Simplified hysteresis model of LCF PMs.

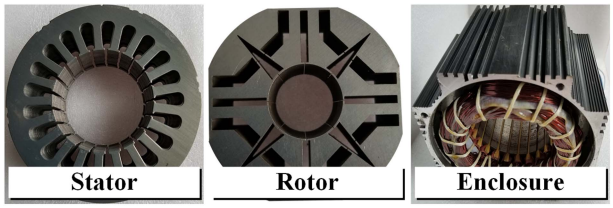

Fig. 4. Prototype of the studied VFMM.

[30]. These solutions are always composed of multiple layers. The options of the original control set are filtered in the front layer(s) by using, for example, the DB [29] and sliding-mode [30] concepts, coming up with a less-option subset addressed in the final layer. In our prestudy [31], a geometric modulation method is used to extend the control set, and an effective three-layer optimization strategy is proposed and verified using simulations. This work follows the prestudy and provides more comprehensive experimental results.

In summary, this article presents a systematic study for applying FS-MPCC to VFMM drives. The main contributions are as follows.

1) A simple measuring procedure is designed for VFMMs to obtain the data of electromagnetic parameters, which are used in FS-MPCC for robustness enhancement.
2) An improved mathematical model is proposed to strengthen the performance of FS-MPCC during flux-regulation processes by considering the induced voltage caused by the rapidly varied PM flux, which is a distinctive consideration in VFMM drives.
3) An efficient three-layer optimization strategy is proposed for FS-MPCC to deal with an extended control set by using less computational burden, which is further verified by experiments based on the prestudy as in [31].

D. Outline

The rest of this article is organized as follows. In Section II, the topology and the principle of PM flux regulation of an HMC-VFMM are described and explained. The measuring procedure of electromagnetic parameters is presented in Section III. Section IV elaborates on the three-layer optimization strategy-based FS-MPCC considering the compensation of induced voltage. In Section V, some experimental results are given to validate the effectiveness of the proposed method. Finally, some conclusions are made in Section VI.

II. HMC-VFMM: Topology and Principle of PM Flux Regulation

A. Topology

The HMC-VFMM proposed in [15] is investigated in this article. The topology of the machine is shown in Fig. 2. As seen, both HCF and LCF PMs, i.e., NdFeB and AlNiCo magnets, are arranged in the rotor, forming a hybrid parallel/series magnetic circuit. This arrangement can combine the advantages of two kinds of magnetic circuits. The HCF PMs in the series branch, on the one hand, can effectively enhance the on-load demagnetization capability of the LCF PMs. On the other hand, the HCF PMs in the parallel branch can be short-circuited within the rotor core when the LCF PMs are reverse magnetized, widening the adjusting range of the air-gap flux. Besides, the designed q-axis flux barriers can effectively mitigate the cross-coupling effect between the d- and q-axis magnetic circuits. Therefore, the mutual inductances are omitted from consideration in this article.

B. Principle of PM Flux Regulation

The existence of LCF PMs gives VFMMs the capacity of online regulating the air-gap flux. The principle can be illustrated by using a simplified hysteresis model of LCF PMs, as shown in Fig. 3. The initial operating point is assumed to be P_0. Applying a negative d-axis current can force the operating point to go below the knee point of the B-H curve and move along the demagnetization line. The operating point will reach a certain point on the demagnetization line (e.g., Q_1) according to the negative d-axis current value, and it will move along a recoil line to a new point on the load line (e.g., P_1) when the injected current is removed. The remagnetization process can be analyzed similarly, such as from P_1 through Q_2 to P_2.

C. Prototype of the Studied HMC-VFMM

The prototype of the studied HMC-VFMM is exhibited in Fig. 4. The main parameters are tabulated in Table I Note that an incremental encoder with 2500 lines has been integrated into the machine casing for sampling the rotor position. The electromagnetic parameters, namely PM flux and dq-axis inductances, will be detailed in Section III.

TABLE I
MAIN PARAMETERS OF THE STUDIED VFMM

Symbol	Quantity	Value
V_{dc}	dc-link voltage	100 V
P_N	Rated power	500 W
n_N	Rated speed	800 r/min
n_p	Pole pairs	2
I_N	Rated current	7.5 A
R_s	Stator resistance	1.3 Ω

TABLE II
SECTOR DETERMINATION

Order of cost function values	Sector
$g(V_1) < g(V_3) < g(V_5)$	I
$g(V_3) < g(V_1) < g(V_5)$	II
$g(V_3) < g(V_5) < g(V_1)$	III
$g(V_5) < g(V_3) < g(V_1)$	IV
$g(V_5) < g(V_1) < g(V_3)$	V
$g(V_1) < g(V_5) < g(V_3)$	VI

III. MEASUREMENT OF ELECTROMAGNETIC PARAMETERS

This section expatiates the simple measuring procedure for electromagnetic parameters of the studied HMC-VFMM, including PM flux and *dq*-axis inductances.

A. *Measurements of PM Flux and* d*-Axis Inductance*

The PM flux and *d*-axis inductance are tested based on the voltage injection method [21]. During this test, the machine rotor should be locked at a known position to inject the *d*-axis voltage. For the sake of simplification, a small positive current (2 A used in experiments) is injected into the winding of *a*-phase to align the *d*-axis of the rotor with the *a*-axis, by doing so, the rotor position can be forced at 0°. Then, the rotor is locked by applying a static load, which is provided by a magnetic powder brake. In this way, the positive/negative *d*-axis voltage can be easily generated by fully turning on the upper/bottom switch of the *a*-phase and the bottom/upper switches of *b* and *c* phases, without needing a closed-loop control of the *q*-axis current. At the same time, the dead-time effect of the inverter [32] can be avoided.

As the machine rotor is stationary, the *d*-axis flux can be expressed by

$$\psi_d = \psi_0 + \int (u_d - R_s i_d)\, dt \tag{1}$$

where ψ_d is the *d*-axis flux, ψ_0 is the dc offset value, which is equal to the value of PM flux, and u_d and i_d are the *d*-axis voltage and the *d*-axis current, respectively.

For instance, the experimental curves of u_d and i_d during the remagnetization operation with a +30 A *d*-axis current injected are presented in Fig. 5(a). It starts by injecting a +100 V *d*-axis voltage to excite the current, and the voltage polarity reverses when the current attains +30 A. The voltage keeps till the current backs to 0. According to the obtained data of u_d and i_d, the curve of *d*-axis flux during the remagnetization process can be obtained, as given in Fig. 5(b). It shows that an increase

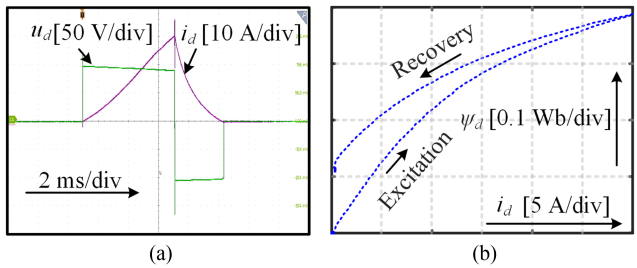

Fig. 5. Experimental results of the remagnetization operation by injecting a +30 A *d*-axis current. (a) Curves of u_d and i_d. (b) Curves of *d*-axis flux.

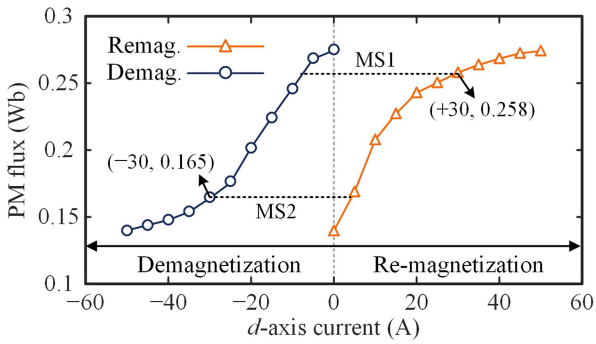

Fig. 6. Re-/demagnetization characteristics of the studied VFMM.

of the *d*-axis flux occurs after the current injection, which is exactly the increment of PM flux because it is increasing and constant during the excitation and recovery stages of the *d*-axis current, respectively. This lays the foundation of the PM flux measurement.

To measure the change curve of the PM flux, a large negative *d*-axis current pulse is injected to sufficiently demagnetize the machine at first, and the back EMF in this condition is tested to determine the initial PM flux. Then, a positive *d*-axis current pulse with a peak value of 5 A is injected. By integrating the recorded data of u_d and i_d, the increment of PM flux can be calculated. The peak value is increased by 5 A each time, and the integration operation is repeated until the increment of PM flux shows a tendency to converge. The peak value of the pulse is up to 50 A and the remagnetization characteristic is described in Fig. 6 by using the orange line. Similarly, the demagnetization characteristic can be acquired by injecting negative *d*-axis current pulses. The peak value of pulse is up to 50 A as well and the demagnetization characteristic curve is shown in Fig. 6 by using the dark blue line.

From Fig. 6, it can be observed that the increase of PM flux is not significant when the current peak value is higher than +30 A. Injecting a +50 A current pulse merely leads to about 3% rate of increase in the PM flux, with respect to the value corresponding to +30 A. By making a tradeoff between the maximum current and PM flux adjusting range, +30 A (four times the rated current value) is selected as the upper limit value of *d*-axis current. The corresponding maximum PM flux is about 0.259 Wb, which is called magnetization state one (MS1). Similarly, the lower limit of *d*-axis current is set to −30 A to achieve a minimum PM flux of 0.138 Wb, called MS2.

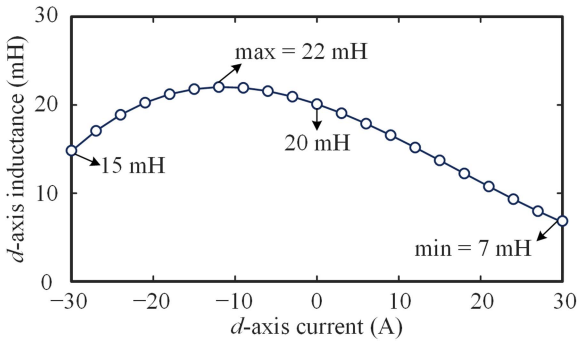

Fig. 7. Relationship between the d-axis inductance and the d-axis current.

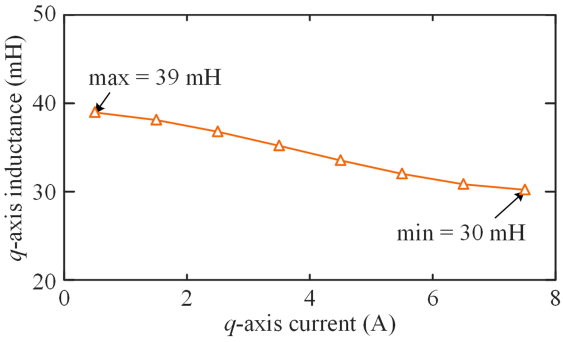

Fig. 8. Relationship between the q-axis inductance and the q-axis current.

Based on the results of PM flux, the d-axis inductance can be easily obtained. Comparatively, this test is relatively effortless. Note that the test of d-axis inductance should be conducted considering the effective range of d-axis current (from -30 to $+30$ A). Thus, before the test a -30 A d-axis current is injected to set the machine at MS2. Then, a $+30$ A d-axis current is injected to obtain the corresponding data of u_d and i_d during the remagnetization process from MS2 to MS1, following which, a -30 A d-axis current is imposed for the demagnetization operation. Calculating the d-axis flux and extracting the PM flux from it, the d-axis flux due to stator excitation (i.e., $\psi_{sd} = L_d i_d$) can be acquired, and the relationship between the d-axis inductance and d-axis current can be then calculated, as provided in Fig. 7.

B. Measurement of q-Axis Inductance

Utilizing the voltage injection method to measure the q-axis inductance needs a closed-loop control for the d-axis current and a large static load to lock the machine rotor. Fortunately, different from the d-axis current, the q-axis component is normally smaller than the rated value (7.5 A). As a consequence, it is feasible to obtain the q-axis inductance online. This work adopts a flux observer to measure the q-axis inductance.

The adopted flux observer is based on the well-known voltage model in the $\alpha\beta$ frame as

$$\begin{cases} \psi_\alpha = \int (u_\alpha - R_s i_\alpha)\, dt \\ \psi_\beta = \int (u_\beta - R_s i_\beta)\, dt \end{cases} \tag{2}$$

where ψ_α and ψ_β are the $\alpha\beta$-axis fluxes, u_α and u_β are the $\alpha\beta$-axis voltages, and i_α and i_β are the $\alpha\beta$-axis currents.

A significant issue using the voltage model is the existence of dc offsets. Considering that the integrated variables are sinusoidal, a second-order generalized integrator (SOGI) is a good choice to deal with both low and high-frequency components (e.g., dc offsets and sampling harmonics). The transfer function of SOGI is

$$G_{\text{SOGI}}(s) = \frac{k\omega_0 s}{s^2 + k\omega_0 s + {\omega_0}^2} \tag{3}$$

where k is a tunable coefficient, and $\omega_0 = 2\pi f_0$ (f_0 is the center frequency) should be equal to the electric angular velocity ω_e.

The filtered $\alpha\beta$-axis fluxes are then transferred to dq-axis components, which is

$$\begin{bmatrix} \psi_d \\ \psi_q \end{bmatrix} = \boldsymbol{T}_{\alpha\beta/dq} \begin{bmatrix} G_{SOGI}\psi_\alpha \\ G_{SOGI}\psi_\beta \end{bmatrix} \tag{4}$$

where ψ_q is the q-axis flux and $\boldsymbol{T}_{\alpha\beta/dq}$ is the transformation from the $\alpha\beta$ frame to the dq frame.

In theory, SOGI does not cause any phase lag of the filtered signal. However, due to the limited sampling frequency in digital implementation, there always exists a nonnegligible phase lag in the output. Thus, a modification of the obtained dq-axis fluxes should be taken into account. Under $i_d = 0$ operation, it is true that ψ_d is equal to ψ_{PM}. Thus, the actual ψ_q can be corrected by

$$\psi_{qc} = \sqrt{\psi_d^2 + \psi_q^2 - \psi_{PM}^2} \tag{5}$$

where ψ_{qc} is the corrected q-axis flux.

Finally, the q-axis inductance can be obtained by using

$$L_q = \frac{\psi_{qc}}{i_q}. \tag{6}$$

In experiments, the studied VFMM rotates at 500 r/min, and the load varies in the range from 0 to the rated value. The relationship between the q-axis inductance and q-axis current is described in Fig. 8.

IV. Proposed FS-MPCC

The aforementioned electromagnetic parameters are stored in LUTs and online utilized in the proposed FS-MPCC, to enhance the robustness. This section explains the other improvements in the proposed control method, including an improved mathematical model considering the induced voltage caused by the rapidly changed PM flux and an effective three-layer optimization strategy to deal with an extended control set using less computational burden.

A. Improved Mathematical Model

The mathematical model of the HMC-VFMM is nearly the same as for a traditional PMSM. In the dq-frame, the voltage equation can be expressed by

$$\begin{bmatrix} u_d \\ u_q \end{bmatrix} = R_s \begin{bmatrix} i_d \\ i_q \end{bmatrix} + \frac{d}{dt} \begin{bmatrix} \psi_d \\ \psi_q \end{bmatrix} + \begin{bmatrix} 0 & -\omega_e \\ \omega_e & 0 \end{bmatrix} \begin{bmatrix} \psi_d \\ \psi_q \end{bmatrix} \tag{7}$$

with

$$\begin{bmatrix}\psi_d\\ \psi_q\end{bmatrix}=\begin{bmatrix}\psi_{sd}\\ \psi_{sq}\end{bmatrix}+\begin{bmatrix}\psi_{\mathrm{PM}}\\ 0\end{bmatrix}=\begin{bmatrix}L_d & 0\\ 0 & L_q\end{bmatrix}\begin{bmatrix}i_d\\ i_q\end{bmatrix}+\begin{bmatrix}\psi_{\mathrm{PM}}\\ 0\end{bmatrix} \tag{8}$$

where u_q is the q-axis voltage, and ψ_{sq} is the q-axis flux due to stator excitation.

For a traditional PMSM, the PM flux ψ_{PM} is deemed as a constant, so that $d\psi_d/dt = d\psi_{sd}/dt$. Differently, the PM flux of VFMM rapidly changes during flux-regulation processes. This means the term $d\psi_{\mathrm{PM}}/dt$ (namely the induced voltage resulting from the change of PM flux) cannot be neglected. Thus, a modified model is proposed in [20] by introducing the induced voltage into the d-axis equation as

$$u_d = Ri_d + L_d\frac{di_d}{dt} - \omega_e L_q i_q + u_{\mathrm{PM}} \tag{9}$$

where

$$u_{\mathrm{PM}} \triangleq \frac{d\psi_{\mathrm{PM}}}{dt} = \frac{d\psi_{\mathrm{PM}}}{di_d}\frac{di_d}{dt}. \tag{10}$$

In [20], the data of $d\psi_{\mathrm{PM}}/di_d$ are obtained by the FE method and stored in LUTs, which needs a lot of effort for the data acquisition. In this article, the term $d\psi_{\mathrm{PM}}/di_d$ is defined as an equivalent inductance, dubbed as L_{PM}, since in this form it is highly akin to the definition of inductance. The improved mathematical model can be expressed by a state-space equation as

$$\dot{\boldsymbol{x}} = \boldsymbol{A}\boldsymbol{x} + \boldsymbol{B}\boldsymbol{u} + \boldsymbol{C} \tag{11}$$

with

$$\boldsymbol{x} = \begin{bmatrix}i_d & i_q\end{bmatrix}^T,\ \boldsymbol{u} = \begin{bmatrix}u_d & u_q\end{bmatrix}^T \tag{12}$$

$$\boldsymbol{A} = \begin{bmatrix}-\frac{R_s}{L_d+L_{\mathrm{PM}}} & \frac{\omega_e L_q}{L_d+L_{\mathrm{PM}}}\\ -\frac{\omega_e L_d}{L_q} & -\frac{R_s}{L_q}\end{bmatrix} \tag{13}$$

$$\boldsymbol{B} = \begin{bmatrix}\frac{1}{L_d+L_{\mathrm{PM}}} & 0\\ 0 & \frac{1}{L_q}\end{bmatrix},\ \boldsymbol{C} = \begin{bmatrix}0\\ -\frac{\omega_e\psi_f}{L_q}\end{bmatrix}. \tag{14}$$

In the normal operation, the equivalent inductance L_{PM} is surely equal to 0. During the flux-regulation processes, L_{PM} is dependent on i_d. Taking the demagnetization operation from MS1 to MS2 as an example, the whole process takes three stages, as illustrated in Fig. 9. In the maintenance stage, the PM flux keeps because the current amplitude is lower than the threshold (about 8 A as shown in Fig. 5). Thereafter, in the regulation stage, the PM flux linearly decreases with the reduced current, until the current reaches the desired value. Finally, in the recovery stage, the PM flux can stabilize at the desired value. What can be noticed is that the term $d\psi_{\mathrm{PM}}/di_d$ is obvious only for the regulation stage, and it is approximately linear. Therefore, the equivalent inductance can be assumed to be a constant during the regulation stage and is considered as 0 for the other two stages. This constant can be solved by

$$L_{\mathrm{PM}} = \frac{\psi_{\mathrm{PM}}^{\mathrm{tgt}} - \psi_{\mathrm{PM}}^{\mathrm{pre}}}{i_d^p - i_d^{ts}} \tag{15}$$

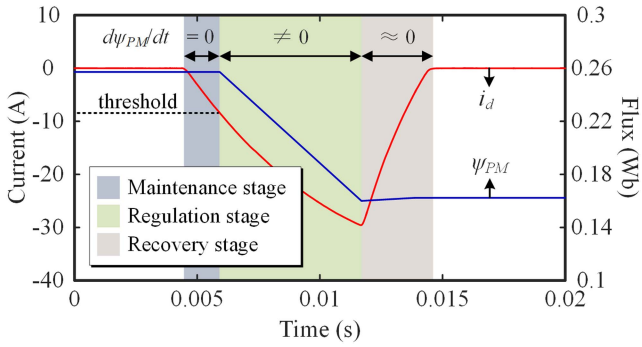

Fig. 9. Illustration of the d-axis current and the PM flux during the demagnetization process from MS1 to MS2.

where $\psi_{\mathrm{PM}}{}^{\mathrm{tgt}}$ and $\psi_{\mathrm{PM}}{}^{\mathrm{pre}}$ are the targeted and present PM flux values, respectively, and $i_d{}^p$ and $i_d{}^{ts}$ are the peak and threshold values of the d-axis current, respectively.

Regarding the demagnetization operation, the equivalent inductance is about 4.23 mH. As for the remagnetization operation from MS2 to MS1, it is about 3.65 mH.

B. Prediction Model and Cost Function

To implement FS-MPCC, the following three steps are normally designed:

1) forecasting the dq-axis currents to the next sampling period using a prediction model, for each voltage vector, namely $\boldsymbol{V}_i \in \nu = \{\boldsymbol{V}_0, \boldsymbol{V}_1, \ldots, \boldsymbol{V}_7\}$ for a two-level inverter [31];
2) assessing the predicted currents of different voltage vectors by a cost function; and
3) choosing the optimal option with the aid of an optimization strategy.

The prediction model and the cost function are crucial for this method. The prediction model is the discretized form of the mathematical model (11), and according to the forward Euler equation it can be deduced as

$$\begin{aligned}\boldsymbol{x}(k+1|\boldsymbol{V}_i) &= e^{T_s\mathbf{A}}\boldsymbol{x}(k) + T_s[\boldsymbol{B}\boldsymbol{u}(k|\boldsymbol{V}_i) + \boldsymbol{C}]\\ &\approx (1+T_s\boldsymbol{A})\boldsymbol{x}(k) + T_s[\boldsymbol{B}\boldsymbol{u}(k|\boldsymbol{V}_i) + \boldsymbol{C}]\end{aligned} \tag{16}$$

where T_s is the sampling period; k and $k+1$ denote the kth and the $(k+1)$th sampling periods, respectively.

Considering the one-beat delay compensation [32] for digital implementation, the dq-axis currents at $(k+2)$th sampling period can be calculated by

$$\begin{aligned}&\boldsymbol{x}(k+2|\boldsymbol{V}_i)\\ &= (1+T_s\boldsymbol{A})\boldsymbol{x}\left(k+1|\boldsymbol{V}_{opt}^k\right) + T_s[\boldsymbol{B}\boldsymbol{u}(k+1|\boldsymbol{V}_i) + \boldsymbol{C}]\end{aligned} \tag{17}$$

where $\boldsymbol{x}(k+1|\boldsymbol{V}^k{}_{\mathrm{opt}})$ is the predicted value of $\boldsymbol{x}$ considering the optimal voltage vector in the last sampling period (i.e., $\boldsymbol{V}^k{}_{\mathrm{opt}}$).

The cost function is always defined as the 2-norm of the tracking errors of dq-axis currents as

$$g(\boldsymbol{V}_i) = \left|\boldsymbol{x}^{ref} - \boldsymbol{x}(k+2|\boldsymbol{V}_i)\right|_2^2 \tag{18}$$

where $\boldsymbol{x}^{\mathrm{ref}} = [i_d{}^{\mathrm{ref}}, i_q{}^{\mathrm{ref}}]^T$ is the reference. Following this, the optimal choice $\boldsymbol{V}_{\mathrm{opt}}$ can be easily determined by using the

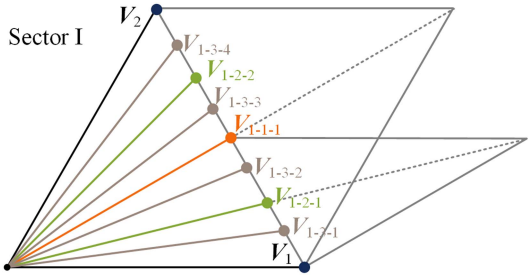

Fig. 10. Construction of virtual vectors in Sector I.

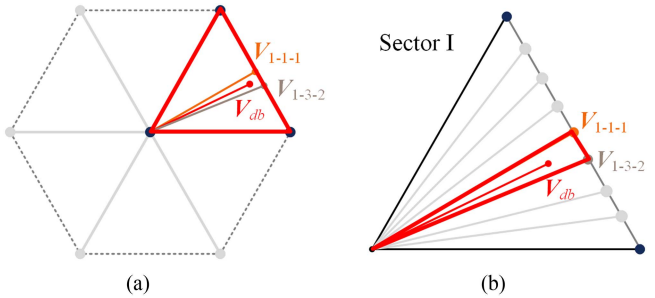

Fig. 11. Principle of the proposed three-layer optimization strategy. (a) Sector determination. (b) Targeted range decision.

enumeration strategy as

$$\boldsymbol{V}_{opt} = \arg\min_{\boldsymbol{V}_i \in \boldsymbol{\nu}} g(\boldsymbol{V}_i) \tag{19}$$

C. Extension of Control Set

Synthesizing basic voltage vectors to construct virtual vectors is a very commonly used way to extend the control set, also known as discrete space vector modulation [33], which is also applied here. According to the principle of vector addition, it is true that two vectors, such as $\boldsymbol{V}_1$ and $\boldsymbol{V}_2$, can be synthesized to yield any vector located at the line between their vertices. For instance, $\boldsymbol{V}_{1\text{-}1\text{-}1}$ and $\boldsymbol{V}_{1\text{-}2\text{-}1}$ shown in Fig. 10 can be obtained by

$$\boldsymbol{V}_{1-1-1}=\frac{1}{2}\boldsymbol{V}_1+\frac{1}{2}\boldsymbol{V}_2 \tag{20}$$

$$\boldsymbol{V}_{1-2-1}=\frac{1}{2}\boldsymbol{V}_1+\frac{1}{2}\boldsymbol{V}_{1-1-1}=\frac{3}{4}\boldsymbol{V}_1+\frac{1}{4}\boldsymbol{V}_2 \tag{21}$$

Other vectors in Fig. 10 can be obtained similarly. A generic expression for vector $\boldsymbol{V}_{j\text{-}m\text{-}n}$ is

$$\boldsymbol{V}_{j-m-n}=\frac{2^m-(2n-1)}{2^m}\boldsymbol{V}_j+\frac{2n-1}{2^m}\boldsymbol{V}_{j+1} \tag{22}$$

where "j" refers to the sector, which determines the two fundamental vectors for the synthetization. "m" shows the iteration steps and "n" defines the order.

It should be mentioned that the illustration in Fig. 10 ends at $m = 3$, whereas the synthetization of vectors is actually an iteration process and can be implemented endlessly. However, the computational burden would be unaffordable if m is too large. For the sake of an affordable computational burden, the maximum iteration step is set as 5 in practice. In this way, the number of virtual vectors in each sector can be increased up to 31 (2^5-1), and hence the total number of options can be extended from 7 to 193.

D. Three-Layer Optimization Strategy

In the traditional FS-MPCC, the optimal vector within the control set is selected by using the enumeration strategy. That is, the prediction model and the cost function are calculated for all options, and then the optimal choice is obtained by comparing the cost function values. However, it will be exactly impracticable due to an unaffordable computational burden if the extended control set with 193 options is considered. In terms of this issue, a three-layer optimization strategy is proposed to replace the inefficient one.

To elaborate the principle of the proposed strategy, the DB vector that makes the cost function (18) equal to zero is highlighted, termed $\boldsymbol{V}_{\rm db}$. The goal is to find the vector closest to $\boldsymbol{V}_{\rm db}$ from the extended control set. The following analyses are also based on $m = 3$, for the sake of a clear presentation. In addition, the DB vector $\boldsymbol{V}_{\rm db}$ locating at Sector I and lying between $\boldsymbol{V}_{1\text{-}2\text{-}1}$ and $\boldsymbol{V}_{1\text{-}3\text{-}2}$ is taken into account for explanation, as seen in Fig. 11(a).

The first layer is to determine the sector. It is confirmed that as for the exampled case in Fig. 11(a), $\boldsymbol{V}_1$ is optimal within the set $\{\boldsymbol{V}_1, \boldsymbol{V}_2, \ldots, \boldsymbol{V}_6\}$, which means the cost function value $g(\boldsymbol{V}_1)$ is smallest. The cost function values rank in the order of $g(\boldsymbol{V}_1)$-$g(\boldsymbol{V}_2)$-$g(\boldsymbol{V}_6)$-$g(\boldsymbol{V}_3)$-$g(\boldsymbol{V}_5)$-$g(\boldsymbol{V}_4)$. If $\boldsymbol{V}_{\rm db}$ is closer to $\boldsymbol{V}_2$ than $\boldsymbol{V}_1$, the order will be $g(\boldsymbol{V}_2)$-$g(\boldsymbol{V}_1)$-$g(\boldsymbol{V}_6)$-$g(\boldsymbol{V}_3)$-$g(\boldsymbol{V}_5)$-$g(\boldsymbol{V}_4)$. Similarly, considering the cases that $\boldsymbol{V}_{\rm db}$ locates at Sector VI, the sort should be $g(\boldsymbol{V}_1)$-$g(\boldsymbol{V}_6)$-$g(\boldsymbol{V}_5)$-$g(\boldsymbol{V}_2)$-$g(\boldsymbol{V}_4)$-$g(\boldsymbol{V}_3)$ or $g(\boldsymbol{V}_6)$-$g(\boldsymbol{V}_1)$-$g(\boldsymbol{V}_5)$-$g(\boldsymbol{V}_2)$-$g(\boldsymbol{V}_4)$-$g(\boldsymbol{V}_3)$. The sort in other manners can be determined in the same way. It can be concluded that the sequence of $g(\boldsymbol{V}_1)$, $g(\boldsymbol{V}_3)$, and $g(\boldsymbol{V}_5)$ is dependent on the sector to be determined, as presented in Table II. Only three vectors need to be calculated in the first layer for sector determination.

The second layer is to determine the targeted range, where only two options are contained [e.g., the range tagged with ($\boldsymbol{V}_{1\text{-}3\text{-}2}$, $\boldsymbol{V}_{1\text{-}1\text{-}1}$), as shown in Fig. 11(b)]. According to (22), each sector is evenly split into several portions by the virtual vectors. Of the two large ranges in Sector I, ($\boldsymbol{V}_1$, $\boldsymbol{V}_{1\text{-}1\text{-}1}$) and ($\boldsymbol{V}_{1\text{-}1\text{-}1}$, $\boldsymbol{V}_2$), the DB vector $\boldsymbol{V}_{\rm db}$ surely lies in ($\boldsymbol{V}_1$, $\boldsymbol{V}_{1\text{-}1\text{-}1}$), which can be validated by $g(\boldsymbol{V}_1) <= g(\boldsymbol{V}_2)$. Then, comparing $g(\boldsymbol{V}_{1\text{-}1\text{-}1})$ and $g(\boldsymbol{V}_1)$ can further verify the range ($\boldsymbol{V}_{1\text{-}2\text{-}1}$, $\boldsymbol{V}_{1\text{-}1\text{-}1}$) embracing $\boldsymbol{V}_{\rm db}$. Finally, the targeted range can be narrowed down to ($\boldsymbol{V}_{1\text{-}3\text{-}2}$, $\boldsymbol{V}_{1\text{-}1\text{-}1}$) according to the comparison between $g(\boldsymbol{V}_{1\text{-}2\text{-}1})$ and $g(\boldsymbol{V}_{1\text{-}1\text{-}1})$. It is worth noting that each division requires only one calculation of the cost function. Such as, to acquire ($\boldsymbol{V}_1$, $\boldsymbol{V}_{1\text{-}1\text{-}1}$), $g(\boldsymbol{V}_2)$ should be calculated and compared with $g(\boldsymbol{V}_1)$ that has been known in the first layer. In summary, the number of vectors considered in the second layer is 3, which accords to the iteration step m.

The third layer is to confirm the superior option between $\boldsymbol{V}_{1\text{-}3\text{-}2}$ and $\boldsymbol{V}_{1\text{-}1\text{-}1}$. To this end, $g(\boldsymbol{V}_{1\text{-}3\text{-}2})$ should be obtained and compared with $g(\boldsymbol{V}_{1\text{-}1\text{-}1})$. Finally, the optimal option termed

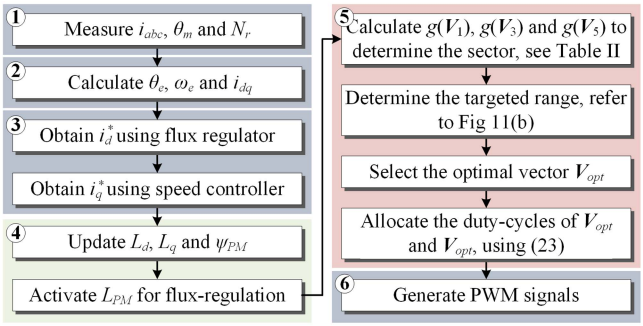

Fig. 12. Implementation flowchart of the proposed FS-MPCC.

$\boldsymbol{V}_{\rm opt}$ can be determined. Overall, considering the case $m = 3$ and omitting the zero vector (i.e., the number of options is 48), only 7 cost function values are needed to accomplish the optimizing process. If $m = 5$, only 9 cost function values are required. In this way, the computational burden can be extremely alleviated.

E. Insertion of Zero Vector

As for FS-MPCC methods, the steady-state performance improvement by applying multivectors has been widely studied. In this article, the zero vector ($\boldsymbol{V}_0$) is used together with the nonzero one ($\boldsymbol{V}_{\rm opt}$) selected by the proposed three-layer optimization strategy. In this manner, a new issue is to allocate the durations of two vectors, which can be effectively addressed by the low-computation duty-cycle calculation algorithm [28]. The duty-cycle calculation is transformed into an optimization problem and can be solved by the well-known Lagrange multiplier method. By this algorithm, the duty cycles of $\boldsymbol{V}_{\rm opt}$ and $\boldsymbol{V}_0$ can be calculated as

$$\begin{cases} d_{opt} = \frac{g(\boldsymbol{V}_0)}{g(\boldsymbol{V}_0)+g(\boldsymbol{V}_{opt})} \\ d_0 = \frac{g(\boldsymbol{V}_{opt})}{g(\boldsymbol{V}_0)+g(\boldsymbol{V}_{opt})} \end{cases} \tag{23}$$

where $d_{\rm opt}$ and d_0 are the duty cycles of $\boldsymbol{V}_{\rm opt}$ and $\boldsymbol{V}_0$, respectively.

F. Implementation of the Proposed FS-MPCC

The implementation of the proposed FS-MPCC method is summarized in a flowchart and a control diagram, as shown in Figs. 12 and 13, respectively. The following six steps are required to be executed.

Step 1: Sample the information of stator currents (i_a, i_b, and i_c) and rotor mechanical angle (θ_m) and speed (N_r).

Step 2: Calculate the electrical angle (θ_e) and electrical angular velocity (ω_e), and compute the dq-axis currents (i_d and i_q) using Park's transformation.

Step 3: Obtain the dq-axis current references ($i_d{}^*$ and $i_q{}^*$) by the flux regulator and the outer speed controller.

Step 4: Update the electromagnetic parameters (L_d, L_q, and $\psi_{\rm PM}$) according to LUTs, and activate the equivalent inductance ($L_{\rm PM}$) during flux-regulation processes.

TABLE III
TESTED METHODS

Method	Control set	Parameters	Optimization strategy
method #1	original	fixed	enumeration
method #2	extended, $m = 3$	measured	three-layer
method #3	extended, $m = 5$	measured	three-layer

Step 5: Select the optimal vector $\boldsymbol{V}_{\rm opt}$ by the proposed three-layer optimization strategy, and allocate the duty cycles by using (23).

Step 6: Transform the duty cycles of vectors to PWM signals for three-phase legs of the inverter.

V. Experimental Verification

An experimental test rig is established to verify the effectiveness of the proposed FS-MPCC, as shown in Fig. 14. The load is provided by a magnetic powder brake, which is mechanically coupled with the tested HMC-VFMM. The tested machine is driven by a customized voltage source inverter consisting of three FF300R12ME4 modules (Infineon). An adjustable dc power supply (100 V/10 A) is in the dc-link and connects with an electrolytic capacitor (450 V/4700 μF) in parallel. The capacitor is indispensable to compensate for the deficiency in terms of the maximum output current of the dc power supply, as the peak value of the d-axis current can be up to 30 A during flux-regulation operations. Furthermore, the stator currents and the dc-link voltage are sampled by three current sensors HAS 50-S (LEM) and a voltage sensor LV25-P (LEM), respectively. The rotor position is sampled by the integrated encoder. All sensed signals are handled by operational amplifier-based adjusting circuits and then fed into a digital signal processor (DSP) TMS320F28335 (TI). The real-time programs are developed in C language on the TI official software Code Composer Studio 7.4.0.

Three control methods are conducted for performance comparison, as presented in Table III. The traditional FS-MPCC is termed method #1, which takes fixed dq-axis inductances ($L_d = 20$ mH and $L_q = 39$ mH) and the original control set (i.e., $\nu = \{\boldsymbol{V}_0, \boldsymbol{V}_1, \ldots, \boldsymbol{V}_7\}$). In addition, two versions of the proposed method are carried out, called method #2 and method #3, which are with $m = 3$ and $m = 5$, respectively. For all tested methods, both the sampling frequency and the control frequency are set to 10 kHz, namely the sampling period $T_s = 100$ μs.

A. Steady-State Performance

The steady-state performance is tested under a speed command of 300 revolutions per minute (r/min) with a 5 N·m load. The curves of stator current of phase-A (i_a) and dq-axis currents (i_d and i_q) and the results of stator current total harmonic distortion (THD) obtained by fast Fourier transformation are provided in Fig. 15. What can be observed is that the stator current can be regulated to be sinusoidal by all three methods. Compared to method #1, the ripples of dq-axis currents can be effectively

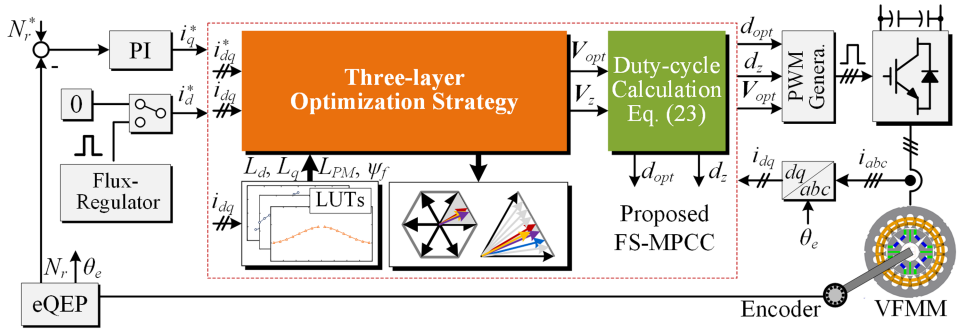

Fig. 13. Control diagram of the proposed method.

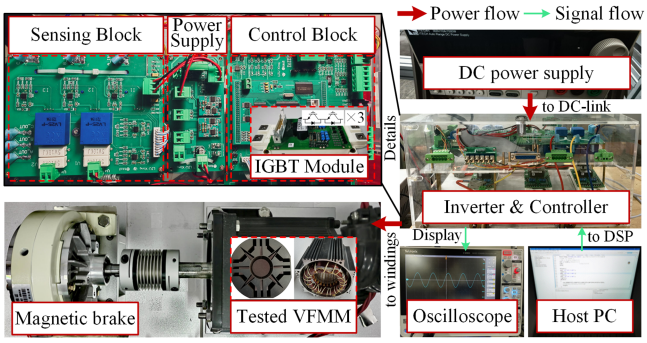

Fig. 14. Experimental test rig.

reduced by using methods #2 and #3. The improvement is more visible for method #3 due to the increase of the iteration step m. From the THD results, the differences in terms of two aspects can be observed. On the one hand, the low-frequency harmonics in the spectrum are in particular significant for method #1, while they are highly suppressed in methods #2 and #3. On the other hand, the content of harmonics around the switching frequency is more pronounced for methods #2 and #3. This means that the inverter can operate more regularly by the proposed method, which is advantageous to noise rejection. It is worth noting that the small switching-frequency harmonic content for method #1 is because of the dead-time effect of the inverter.

The stator current THDs under different load conditions are attested in a manner where the machine rotates at 300 r/min, as given in Fig. 16. The load torque is adjusted from 0 to 6 N·m (0 to 1 p.u.). Notice that due to the friction, the current is not zero when the load is disabled. As seen, in the whole load torque range, the performance of method #1 is at the bottom while method #3 ranks first. The difference narrows down as the load torque increases. The THD results of the three methods in the load torque range from 0.5 to 1 p.u. are zoomed in. As observed, the performance of methods #2 and #3 is very similar to each other, and both of them are superior to method #1 significantly.

B. Dynamic Performance

In terms of dynamic performance, the flux-regulation operations are considered. The d-axis current reference is given in a step-change manner. The remagnetization operation from MS2 to MS1 is conducted under a speed command of 300 r/min with a 5 N·m load (namely a low-speed heavy-load condition). The results are given in Fig. 17. As seen, all three methods perform well in terms of dynamic response. Comparatively, as the induced voltage term is not considered in method #1, a small overshoot is resulted. The current can be controlled precisely without any overshoot in methods #2 and #3.

The demagnetization operation from MS1 to MS2 is carried out under a speed command of 600 r/min with a 2 N·m load (i.e., a high-speed light-load condition). The results are presented in Fig. 18. Also, the overshoot is only seen in method #1. The response processes of the three methods are basically similar. It should be noted that the demagnetization operations take longer time than the remagnetization operations. This difference can be explained by the characteristic of d-axis inductance, as shown in Fig. 7. In summary, the results in relation to flux regulation show the effectiveness of the improved model considering the induced voltage proposed in Section III-A. Meanwhile, the proposed FS-MPCC method takes a similar dynamic performance to the traditional FS-MPCC.

C. Robustness Verification

From Fig. 8, it is observed that the q-axis inductance changes within the range from 30 to 39 mH, according to the q-axis current value. Noting this, the q-axis current ripples of the three methods are measured under different load conditions with a speed command of 300 r/min, to compare the robustness. The results are shown in Fig. 19, where 1 p.u. also corresponds to 6 N·m. As described, the q-axis current ripple for method #2 is almost unchanged with the working condition, as well as for method #3, which is because LUTs are used to update the q-axis inductance. Differently, the q-axis current ripple for method #1 severely increases with the load. Actually, the magnetic circuit saturation effect under heavy load conditions leads to a smaller q-axis inductance. As such, the q-axis current is predicted in a seriously wrong manner, leading to a larger current ripple.

D. Computational Burden Comparison

Finally, the computational burdens of the three methods are measured and compared. Considering the control frequency of 10 kHz, there are 15000 clock cycles available for each control period, as the DSP TMS320F28335 has the main frequency of

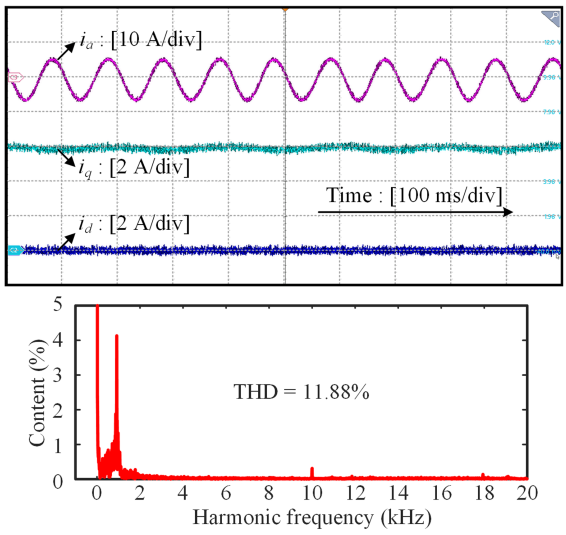

(a)

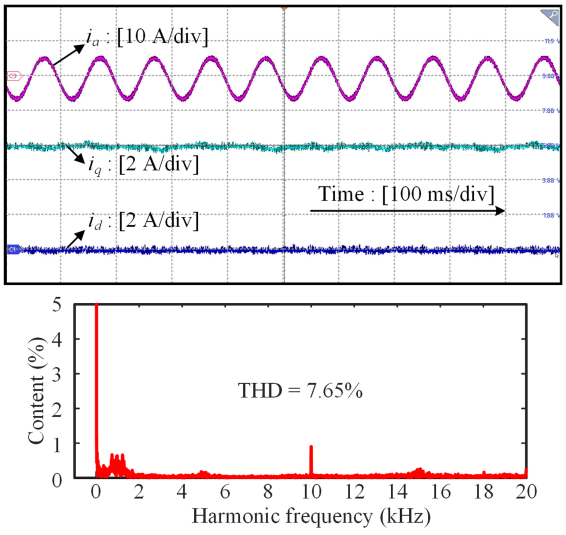

(b)

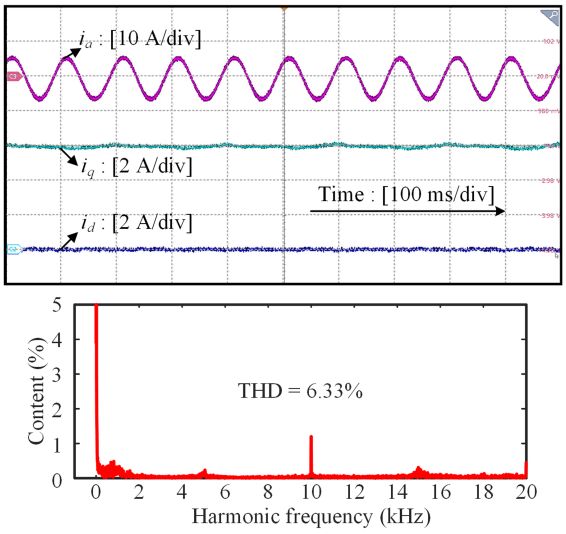

(c)

Fig. 15. Experimental results under steady-state conditions (300 r/min, 5 N·m). (a) Method #1. (b) Method #2. (c) Method #3.

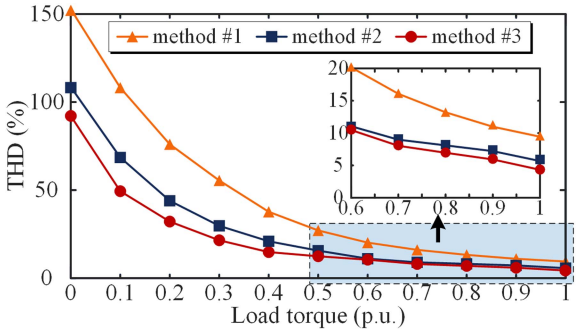

Fig. 16. Stator current THDs under different load conditions at 300 r/min.

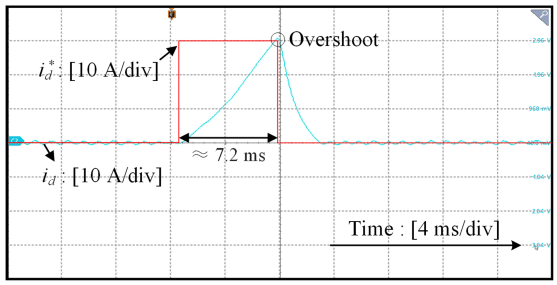

(a)

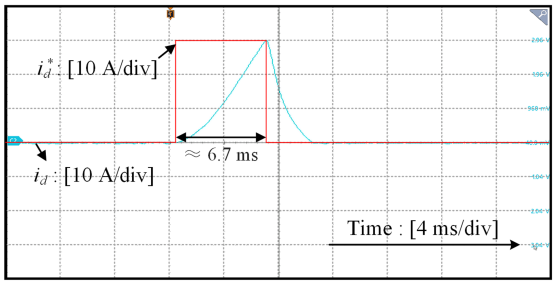

(b)

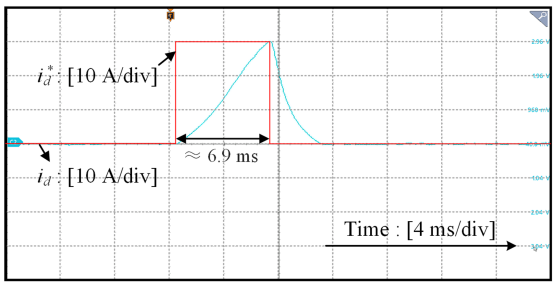

Fig. 17. Experimental results of remagnetization operation from MS2 to MS1 (100 r/min, 5 N·m). (a) Method #1. (b) Method #2. (c) Method #3.

150 MHz. To sample the spent clock cycles, two breakpoints are set at the beginning and the ending of each code to be assessed, respectively. In addition to the tested three methods, methods #2 and #3 with the enumeration strategy are also conducted, termed method #2* and method #3*, respectively. The execution time for implementing the five methods and their individual optimization strategies is summarized in Fig. 20. As seen, 39.15 μs, 46.51 μs, 49.09 μs, 67.85 μs, and 344.52 μs are required for the five methods to be implemented, respectively.

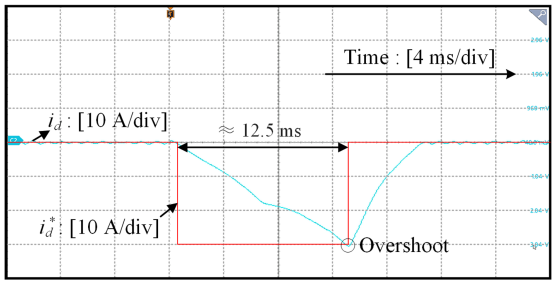

(a)

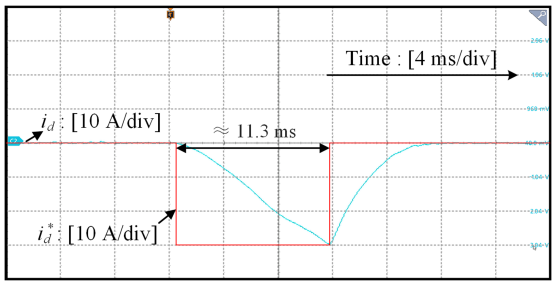

(b)

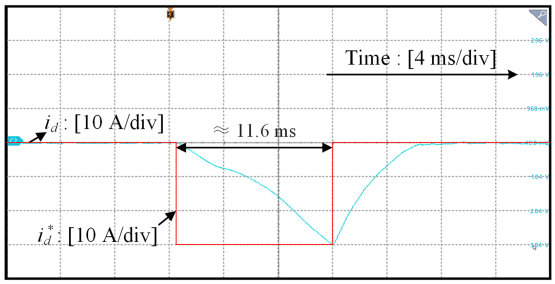

(c)

Fig. 18. Experimental results of demagnetization operation from MS1 to MS2 (600 r/min, 2 N·m). (a) Method #1. (b) Method #2. (c) Method #3.

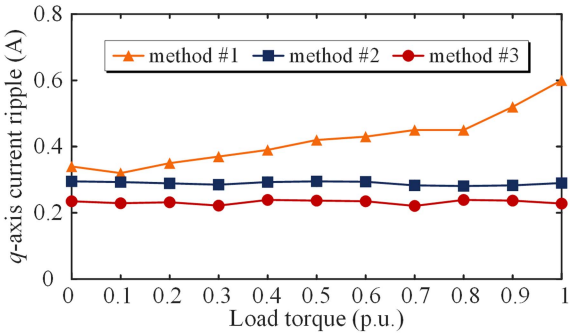

Fig. 19. Ripple of q-axis current under different load conditions at 300 r/min.

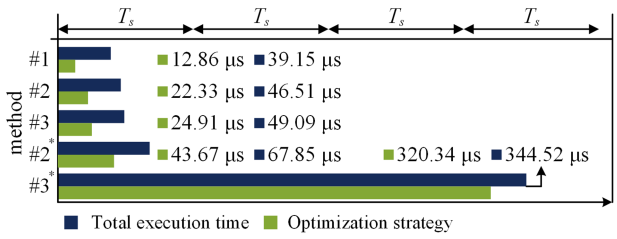

Fig. 20. Experimental results of computational burden.

The execution time of the optimization strategies used in five methods accounts for 32.85%, 48.01%, 50.74%, 64.36%, and 92.98% of the total execution time, respectively. In cases of $m = 3$ and $m = 5$, the extended control set is with 24 and 192 options, respectively, and the execution time to select the best by the enumeration strategy is up to 43.67 μs and 320.34 μs, which is exactly unacceptable. With the proposed three-layer optimization strategy, the execution time of optimization can be reduced by about 48.87% and about 92.22%, respectively. This indicates that the proposed three-layer optimization strategy is highly efficient over the enumeration strategy.

VI. Conclusion

In this article, a systematic study of applying FS-MPCC to VFMM drives is presented. A simple measuring procedure of electromagnetic parameters is designed. On this foundation, a novel three-layer optimization strategy-based FS-MPCC method with enhanced robustness and improved steady-state performance is proposed, which is verified by comprehensive experiments. The results show the advantages of the proposed method, as follows.

1) The proposed FS-MPCC is with better steady-state performance compared to the traditional one. Not only the low-frequency harmonics can be suppressed, but also the switching frequency-related harmonics are more visible.
2) The dynamic performance of the proposed FS-MPCC is comparable to the traditional one. Meanwhile, due to the consideration of induced voltage, the proposed method can well regulate the d-axis current during flux-regulation processes, without any overshoot.
3) The proposed FS-MPCC has better robustness than the traditional one since LUTs are used to update the electromagnetic parameters. The performance of the proposed method is almost unchanged with the working conditions.
4) The proposed three-layer optimization strategy is highly efficient over the enumeration strategy. Moreover, the reduction of computational burden is becoming more conspicuous with the increase of iteration step.

References

[1] Z. Q. Zhu and D. Howe, "Electrical machines and drives for electric, hybrid, and fuel cell vehicles," *Proc. IEEE*, vol. 95, no. 4, pp. 746–765, Apr. 2007.
[2] C. Liu, K. T. Chau, C. H. T. Lee, and Z. Song, "A critical review of advanced electric machines and control strategies for electric vehicles," *Proc. IEEE*, vol. 109, no. 6, pp. 1004–1028, Jun. 2021.
[3] D. Egorov et al., "Hysteresis loss in NdFeB permanent magnets in a permanent magnet synchronous machine," *IEEE Trans. Ind. Electron.*, vol. 69, no. 1, pp. 121–129, Jan. 2022.
[4] J. Cekani, F. Capponi, G. Donato, and F. Caricchi, "Mechanical flux weakening methods for the achievement of a very wide constant power speed range in automotive applications," *IEEE J. Emerg. Sel. Top. Power Electron.*, vol. 10, no. 3, pp. 3443–3458, Jun. 2022.
[5] S. Liu, Z. Song, Y. Liu, Y. Chen, and C. Liu, "Flux-weakening controller design of dual three-phase PMSM drive system with copper loss minimization," *IEEE Trans. Power Electron.*, vol. 38, no. 2, pp. 2351–2363, Feb. 2023.
[6] H. Yang, Z. Q. Zhu, H. Lin, and W. Chu, "Flux adjustable permanent magnet machines: A technology status review," *Chin. J. Elect.*, vol. 2, no. 2, pp. 14–30, Dec. 2016.

[7] H. Xu, J. Li, J. Chen, Y. Lu, and M. Ge, "Analysis of a hybrid permanent magnet variable-flux machine for electric vehicle tractions considering magnetizing and demagnetizing current," *IEEE Trans. Ind. Appl.*, vol. 57, no. 6, pp. 5983–5992, Nov./Dec. 2021.
[8] A. Athavale, K. Sasaki, B. S. Gagas, T. Kato, and R. D. Lorenz, "Variable flux permanent magnet synchronous machine (VF-PMSM) design methodologies to meet electric vehicle traction requirements with reduced losses," *IEEE Trans. Ind. Appl.*, vol. 53, no. 5, pp. 4318–4326, Sep./Oct. 2017.
[9] S. Maekawa et al., "Study of the magnetization method suitable for fractional-slot concentrated-winding variable magnetomotive-force memory motor," *IEEE Trans. Power Electron.*, vol. 29, no. 9, pp. 4877–4887, Sep. 2014.
[10] R. Tu, H. Yang, H. Lin, H. Zhan, D. Wu, and M. Yu, "Design and optimization of a novel delta-type consequent-pole hybrid magnet memory machine," *IEEE Trans. Energy Convers.*, vol. 39, no. 2, pp. 1265–1277, Jun. 2024.
[11] V. Ostovic, "Memory motors," *IEEE Ind. Appl. Mag.*, vol. 9, no. 1, pp. 52–61, Jan./Feb. 2003.
[12] R. Tsunata, M. Takemoto, S. Ogasawara, and K. Orikawa, "Variable flux memory motor employing double-layer delta-type PM arrangement and large flux barrier for traction applications," *IEEE Trans. Ind. Appl.*, vol. 57, no. 4, pp. 3545–3561, Jul./Aug. 2021.
[13] W. Liu, H. Yang, H. Lin, S. Lyu, and Y. Zhong, "A novel variable flux memory machine with separated series–parallel PM structure," *IEEE Trans. Ind. Electron.*, vol. 70, no. 4, pp. 3348–3361, Apr. 2023.
[14] H. Hua, Z. Q. Zhu, A. Pride, R. Deodhar, and T. Sasaki, "Comparative study on variable flux memory machines with parallel or series hybrid magnets," *IEEE Trans. Ind. Appl.*, vol. 55, no. 2, pp. 1408–1419, Mar./Apr. 2019.
[15] H. Yang, S. Lyu, H. Lin, Z. Q. Zhu, H. Zheng, and T. Wang, "A novel hybrid-magnetic-circuit variable flux memory machine," *IEEE Trans. Ind. Electron.*, vol. 67, no. 7, pp. 5258–5268, Jul. 2020.
[16] Y. Zhong, H. Lin, Z. Chen, S. Lyu, and H. Yang, "Online-parameter-estimation-based control strategy combining MTPA and flux-weakening for variable flux memory machines," *IEEE Trans. Power Electron.*, vol. 37, no. 4, pp. 4080–4090, Apr. 2022.
[17] K. Yu and Z. Wang, "Improved deadbeat predictive current control of dual three-phase variable-flux PMSM drives with composite disturbance observer," *IEEE Trans. Power Electron.*, vol. 37, no. 7, pp. 8310–8321, Jul. 2022.
[18] J. Chen, J. Li, and R. Qu, "Maximum-torque-per-ampere and magnetization-state control of a variable-flux permanent magnet machine," *IEEE Trans. Ind. Electron.*, vol. 65, no. 2, pp. 1158–1169, Feb. 2018.
[19] A. Athavale, D. J. Erato, and R. D. Lorenz, "Enabling driving cycle loss reduction in variable flux PMSMs via closed-loop magnetization state control," *IEEE Trans. Ind. Appl.*, vol. 54, no. 4, pp. 3350–3359, Jul./Aug. 2018.
[20] J. Chen, J. Li, and R. Qu, "Analysis, modeling, and current trajectory control of magnetization state manipulation in variable-flux permanent magnet machines," *IEEE Trans. Ind. Electron.*, vol. 66, no. 7, pp. 5133–5143, Jul. 2019.
[21] R. Thike and P. Pillay, "Characterization of a variable flux machine for transportation using a vector-controlled drive," *IEEE Trans. Trans. Electrif.*, vol. 4, no. 2, pp. 494–505, Jun. 2018.
[22] Z. Chen, H. Lin, Y. Zhong, S. Lyu, and H. Yang, "A novel current control strategy for magnetization state manipulation of variable flux memory machine based on linear active disturbance rejection," *IEEE Trans. Power Electron.*, vol. 37, no. 2, pp. 1962–1971, Feb. 2022.
[23] J. Rodriguez et al., "Latest advances of model predictive control in electrical drives—Part I: Basic concepts and advanced strategies," *IEEE Trans. Power Electron.*, vol. 37, no. 4, pp. 3927–3942, Apr. 2022.
[24] J. Rodriguez et al., "Latest advances of model predictive control in electrical drives—Part II: Applications and benchmarking with classical control methods," *IEEE Trans. Power Electron.*, vol. 37, no. 5, pp. 5047–5061, May 2022.
[25] J. Holtz, "Predictive finite-state control—When to use and when not," *IEEE Trans. Power Electron.*, vol. 37, no. 4, pp. 4225–4232, Apr. 2022.
[26] Y. Zhang, J. Jin, and L. Huang, "Model-free predictive current control of PMSM drives based on extended state observer using ultralocal model," *IEEE Trans. Ind. Electron.*, vol. 68, no. 2, pp. 993–1003, Feb. 2021.
[27] Z. Chen, J. Qiu, and M. Jin, "Adaptive finite-control-set model predictive current control for IPMSM drives with inductance variation," *IET Elect. Power Appl.*, vol. 11, no. 5, pp. 874–884, 2017.
[28] F. Yu, X. Liu, Z. Zhu, and J. Mao, "An improved finite-control-set model predictive flux control for asymmetrical six-phase PMSMs with a novel duty-cycle regulation strategy," *IEEE Trans. Energy Convers.*, vol. 36, no. 2, pp. 1289–1299, Jun. 2021.
[29] X. Sun, T. Li, M. Yao, G. Lei, Y. Guo, and J. Zhu, "Improved finite-control-set model predictive control with virtual vectors for PMSHM drives," *IEEE Trans. Energy Convers.*, vol. 37, no. 3, pp. 1885–1894, Sep. 2022.
[30] I. Hassine, M. Naouar, and N. Mrabet-Bellaaj, "Model predictive-sliding mode control for three-phase grid-connected converters," *IEEE Trans. Ind. Electron.*, vol. 64, no. 2, pp. 1341–1349, Feb. 2017.
[31] X. Liu, H. Yang, H. Lin, F. Yu, H. Zhan, and C. Liu, "Finite-set model predictive current control for variable-flux memory machine drives with a three-stage optimization strategy," in *Proc. IEEE Int. Conf. Predictive Control Elect. Drives Power Electron.*, 2023, pp. 1–6.
[32] C. Lim, S. Lee, and E. Levi, "Continuous-control-set model predictive current control of asymmetrical six-phase drives considering system non-idealities," *IEEE Trans. Ind. Electron.*, vol. 70, no. 8, pp. 7615–7626, Aug. 2023.
[33] I. Alsofyani and K. Lee, "A unidirectional voltage vector preselection strategy for optimizing model predictive torque control with discrete space vector modulation of IPMSM," *IEEE Trans. Ind. Electron.*, vol. 69, no. 12, pp. 12305–12315, Dec. 2022.

Xing Liu (Graduate Student Member, IEEE) received the B.Eng. and M.Sc. degrees in electrical engineering from Nantong University, Nantong, China, in 2018 and 2022, respectively. He is currently working toward the Ph.D. degree in electrical engineering with Southeast University, Nanjing, China.

His research interests include the control strategies of power electronics and permanent magnet machines.

Hui Yang (Senior Member, IEEE) received the B.Eng. degree from Dalian University of Technology, Dalian, China, in 2011, and the Ph.D. degree from Southeast University, Nanjing, China, in 2016, respectively, both in electrical engineering.

From 2014 to 2015, he was supported by the China Scholarship Council through a one-year joint Ph.D. studentship with the University of Sheffield, Sheffield, U.K. Since 2016, he has been an Associate Professor with the School of Electrical Engineering, Southeast University. From 2019 to 2020, he was a postdoctoral fellow with the School of Electrical Engineering, The Hong Kong Polytechnic University. He authored or coauthored more than 80 IEEE transactions papers and was a peer reviewer of more than 10 IEEE journals and the holder of 27 patents. His research interests include novel permanent-magnet machines and drives with particular reference to variable-flux machines for electric vehicles and renewable energy applications.

Dr. Yang is currently an Associate Editor for IEEE TRANSACTIONS ON INDUSTRIAL ELECTRONICS and an Editor of the *World Electric Vehicle Journal*. He is also the TPC-Track Chair of IEMDC 2021 and Organizing Committee Chair of CIEEC 2022. He was invited as a tutorial speaker for PESA 2020 and IEMDC 2021. He was the recipient of Best Paper Awards in ICEMS 2014, EVER 2015, ICEMS 2019, and EVS 34.

Heyun Lin (Senior Member, IEEE) received the B.S., M.S., and Ph.D. degrees in electrical engineering from Nanjing University of Aeronautics and Astronautics, Nanjing, China, in 1985, 1989, and 1992, respectively.

From 1992 to 1994, he was a postdoctoral fellow with Southeast University, Nanjing, China. In 1994, he joined the School of Electrical Engineering, Southeast University as an Associate Professor and became a Full Professor in 2000. His research interests include the design, analysis, and control of permanent magnet motors, intelligent electrical apparatus, and electromagnetic field numerical analysis. He is the author of more than 150 technical papers and the holder of 30 patents.

Dr. Lin is a Fellow of IET, a member of the Electrical Motor and Apparatus Committee of Jiangsu Province, and a senior member of both China Society of Electrical Engineering and China Electrotechnical Society.

Feng Yu (Member, IEEE) was born in Suzhou, China, in 1985. He received the B.Eng. degree in electrical engineering and automation from the School of Electrical Engineering, Sanjiang University, Nanjing, China, in 2008, the M.Sc. degree in electrical engineering from the School of Electrical and Information Engineering, Jiangsu University, Zhenjiang, China, in 2011, and the Ph.D. degree in electrical engineering with the Department of Electrical Engineering, Southeast University, Nanjing, China, in 2016.

Since 2016, he has been with Nantong University, Nantong, China, where he is currently a Full Professor in the School of Electrical Engineering. His current research focuses on the control of multiphase machines and drives for applications ranging from automotive to renewable energy.

Yong Yang (Senior Member, IEEE) received the B.S. degree in automation from Xiangtan University, Xiangtan, China, in 2003, the M.S. degree in electrical engineering from Guizhou University, Guiyang, China, in 2006, and the Ph.D. degree in electrical engineering from Shanghai University, Shanghai, China, in 2010.

He is currently a Full Professor with the School of Rail Transportation, Soochow University, Suzhou, China. From 2017 to 2018, he was a Visiting Scholar with the Center for High Performance Power Electronics of The Ohio State University, Columbus, OH, USA. He coauthored more than 100 journal and conference papers. His research interests include model predictive control in power electronic converters, distributed energy resource interfacing, and high-performance motor drive control.